AGU PUBLICATIONS

JGR

Journal of Geophysical Research: Solid Earth

RESEARCH ARTICLE

10.1002/2014JB011135

Key Points:
- We conducted shear deformation experiments using quasi-Maxwell fluids
- Elastic rebounds and viscous relaxation occur for rapid and slow deformations
- At intermediate, rebounds at a shear wave velocity leave unrecoverable strains

Supporting Information:
- Readme
- Movie S1
- Movie S2
- Movie S3
- Movie S4
- Movie S5

Correspondence to:
A. Namiki,
namiki@eps.s.u-tokyo.ac.jp

Citation:
Namiki, A., T. Yamaguchi, I. Sumita, T. Suzuki, and S. Ide (2014), Earthquake model experiments in a viscoelastic fluid: A scaling of decreasing magnitudes of earthquakes with depth, *J. Geophys. Res. Solid Earth*, *119*, 3169–3181, doi:10.1002/2014JB011135.

Received 19 MAR 2014
Accepted 20 MAR 2014
Accepted article online 28 MAR 2014
Published online 14 APR 2014

Earthquake model experiments in a viscoelastic fluid: A scaling of decreasing magnitudes of earthquakes with depth

Atsuko Namiki[1], Tetsuo Yamaguchi[2], Ikuro Sumita[3], Takehito Suzuki[1,4], and Satoshi Ide[1]

[1]Department of Earth and Planetary Science, University of Tokyo, Tokyo, Japan, [2]Department of Mechanical Engineering, School of Engineering, Kyushu University, Fukuoka, Japan, [3]Graduate School of Natural Science and Technology, Kanazawa University, Kanazawa, Japan, [4]Now at Department of Physics and Mathematics, Aoyama Gakuin University, Sagamihara, Japan

Abstract We performed shear deformation experiments using quasi-Maxwell fluids. We found that, depending on the strain rates, the same material generates earthquakes associated with the elastic rebound and deforms viscously. Around the threshold, elastic rebound releases a certain fraction of the interseismic displacement, but the other fraction remains as a result of the viscous relaxation. We applied our experimental results to a subduction zone, in which the upper part of the hanging wall behaves as an elastic layer and generates seismicity, while the deeper part behaves as a viscous fluid and subducts with the slab. Our experimental results suggest that, around the boundary of the elastic and viscous layers, seismicity can occur, but only some part of the interseismic displacements is released. The experimentally obtained threshold of the seismic activity is determined by the combination of the subduction velocity v_s, the viscosity of the hanging wall η, the fault length W, and the adhesive stress σ_a, $v_s\eta/(W\sigma_a) > 1$. This threshold suggests that if the viscosity of the hanging wall decreases with depth, the maximum size of the earthquakes also decreases with depth, and, finally, seismicity disappears. This hypothesis is consistent with the observed fact that slow earthquakes, characterized by their small magnitudes, are observed at the downdip limit of the seismogenic zone.

1. Introduction

Seismic activities along the subducting slab change with depth (Figure 1). The shallowest part is known as the aseismic or tsunamigenic region; beneath it, the seismogenic zone exists, where ruptures for great earthquakes occur. At a sufficiently deep mantle, seismicity disappears [e.g., *Tichelaar and Ruff*, 1983; *Oleskevich et al.*, 1999; *Lay et al.*, 2012; *Hyndman*, 2013]. *Lay et al.* [2012] analyze great earthquakes globally and show that the largest fault displacement associated with ruptures occurs at shallower depths.

Around the downdip limit of the seismogenic zone, slow earthquakes, such as nonvolcanic tremors, low-frequency earthquakes, and slow-slip events, are observed [e.g., *Beroza and Ide*, 2011; *Obara*, 2011]. The displacement associated with individual rupture event of a slow earthquake is smaller than that of ordinary earthquakes observed at shallower depths. The along-strike source region of a tremor has two peaks, and up-dip tremor activity occurs episodically, often correlating with geodetically observed slip [*Wech et al.*, 2009; *Obara et al.*, 2010]. Very low frequency earthquakes, which show relatively larger magnitudes among slow earthquakes, are observed at the up-dip sides of peaks in tremors [*Ito et al.*, 2009; *Obara*, 2011]. These observations suggest that the magnitude of seismicity becomes smaller with depth and disappears at a certain depth.

The rheology of rocks comprising the earth also varies with depth, and layered rheology, in which an elastic plate overlies a viscous (or viscoelastic) layer, is frequently used. Under deformation, an elastic upper layer stores elastic energy. When the elastic stress exceeds the frictional strength of a fault, brittle failures or ruptures occur as sources of seismicity. The frictional strength increases with depth as a function of pressure, whereas the viscous strength decreases with depth as a function of temperature; then rocks deform as a ductile material at a depth, known as the brittle-ductile transition [e.g., *Kohlstedt et al.*, 1995; *Burgmann and Dresen*, 2008]. The rheology of the lower layer may not be a simple Newtonian viscosity [e.g., *Freed et al.*, 2006] and is commonly modeled using Maxwell or Burgers bodies, which respond to a sufficiently slow deformation as a fluidlike material, i.e., permanent displacement can remain without accumulation of elastic

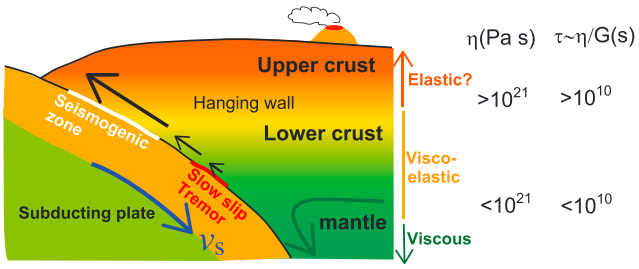

Figure 1. A cross section of a subduction zone. Black arrows indicate decreasing coseismic displacement with depth. Possible viscosity range, η, and relaxation time, $\tau = \eta/G$, are indicated, in which we assume $G \sim 10^{11}$ Pa.

energy [e.g., *Pollitz*, 2003; *Burgmann and Dresen*, 2008; *Wang et al.*, 2012]. This picture has been investigated using dislocation models [*Nur and Mavko*, 1974; *Thatcher et al.*, 1980; *Savage*, 1983; *Burgmann and Dresen*, 2008; *Wang et al.*, 2012].

The rheology of rocks comprising the Earth has been estimated from laboratory rock mechanics experiments and geodetic observations of post-loading strain transients. Laboratory experiments show that lower crust and shallow mantle viscosities can become as low as the order of the magnitude of $\eta \sim 10^{19}$ Pa s, depending on temperature, strain rate, and H_2O [e.g., *Hilairet et al.*, 2007; *Burgmann and Dresen*, 2008; *Hirauchi et al.*, 2010; *Hirschmann and Kohlstedt*, 2012]. A typical viscosity of the upper mantle estimated by glacial isostatic adjustment is the order of the magnitude of $\eta \sim 10^{21}$ Pa s [e.g., *Mitrovica and Forte*, 2004]. The viscosities estimated by geodetic observations for the lower crust and shallow upper mantle are as low as $\eta \sim 10^{19}$ Pa s [e.g., *Thatcher et al.*, 1980; *Nishimura and Thatcher*, 2003; *Hilley et al.*, 2009; *Rousset et al.*, 2012]. Applying the constitutive laws of rocks obtained by laboratory experiments, the viscosity of the shallower elastic layer becomes larger than that of the lower crust because of its low temperature [*Yamasaki and Seno*, 2005; *Muto et al.*, 2013]. We thus consider that the viscosities of the viscous layer (lower crust and shallow upper mantle) and the elastic layer are lower and higher, respectively, than 10^{21} Pa s, as indicated in Figure 1.

Given that a shear modulus is of the order of the magnitude of $G \sim 10^{11}$ Pa [e.g., *Dziewonski and Anderson*, 1981; *Bilek and Lay*, 1999] and is only weakly depth dependent as compared to the viscosity, the relaxation time $\tau = \eta_a/G_a$ which characterizes a Maxwell fluid becomes shorter with depth. Here G_a is the asymptotical rigidity under an infinitely rapid deformation, and η_a is the asymptotical viscosity under an infinitely slow deformation; however, we do not know G_a and η_a, so we assume $G_a \sim G$ and $\eta_a \sim \eta$.

The details of the rheology of the crustal and mantle rocks depend on a number of factors, e.g., temperature, depth, composition, and phase content [e.g., *Burgmann and Dresen*, 2008]. However, using relaxation times as a first-order approximation, we can simply understand the rheological structure of the Earth. The shallower more elastic layer is interpreted as a region with a longer relaxation time, and the deeper more viscous layer is a region with a relatively shorter relaxation time. Since we only considered the effect of the relaxation time, we have not distinguished here the differences between viscous, plastic (power law), and ductile deformations.

Since slow earthquakes are observed around the lower limit of the seismogenic zone, which may be related to the rheological transition, the effect of anelasticity on slow earthquakes has been suggested [e.g., *Nakata et al.*, 2011; *Ando et al.*, 2012]. Viscoelastic rheology explains the propagation velocity of seismic activities [*Ando et al.*, 2012]. On the other hand, the slow rupture velocities of slow earthquakes are modeled by complex frictional characteristics, including fluids and fracturing effects [e.g., *Perfettini and Ampuero*, 2008; *Suzuki and Yamashita*, 2009; *Shibazaki et al.*, 2012; *Colella et al.*, 2013; *Matsuzawa et al.*, 2013]. The complex friction also can cause transition from stable creeping to a dynamic rupturing [*Kuwano and Hatano*, 2011; *Noda and Lapusta*, 2013; *Ujiie et al.*, 2013].

In order to understand the seismogenesis in a viscoelastic material, frictional sliding experiments using viscoelastic gels have been conducted [e.g., *Baumberger et al.*, 2002; *Corbi et al.*, 2011; *Yamaguchi et al.*, 2011; *Corbi et al.*, 2013; *Latour et al.*, 2013a, 2013b]. When a viscoelastic gel slides over a hard plate, it locally detaches from the plate; the propagation of this detachment is known as a Schallamach wave [*Schallamach*, 1971] a self-healing slip pulse [*Baumberger et al.*, 2002], or a wrinkle-like slip pulse [*Andrews and Ben-Zion*, 1997], also known to become a mechanism for reducing frictional heating during an earthquake [*Brune et al.*, 1993].

The gels used in the above experiments as a rock analogue are viscoelastic solids simulating the delay of deformation for rapid deformation; they are not suitable for simulating the disappearance of seismicity

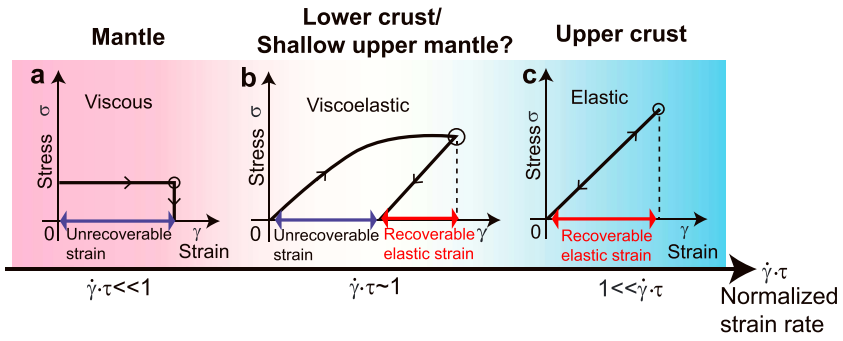

Figure 2. Schematic stress-strain histories for loading and unloading of (a) viscous, (b) viscoelastic, (c) elastic materials; in other words, (Figure 2a) slow, (Figure 2b) intermediate, and (Figure 2c) rapid deformations. Circles indicate unloading. When a constant strain rate $\dot{\gamma}$ is imposed, the strain γ increases with elapsed time. Under a slow deformation $\dot{\gamma}\tau \ll 1$, the stress σ is accommodated in a Maxwell body proportional to the strain rate $\sigma \propto \dot{\gamma}$. When unloading occurs, the accumulated strain remains as indicated by the blue arrow in Figure 2a. In contrast, under a rapid deformation $\dot{\gamma}\tau \gg 1$, the stress increases proportional to the strain γ. When unloading occurs, the accumulated strain recovers, as denoted by the red arrow in Figure 2c. Under an intermediate deformation rate, $\dot{\gamma}\tau \sim 1$, some fraction of the accumulated strain recovers when unloading occurs as denoted by the red and blue arrows in Figure 2b.

by rheological transition. It is known that a Maxwell fluid under a rapid and slow deformation ($\gg 1/\tau$ and $\ll 1/\tau$) behaves like an elastic and viscous media, respectively. At a strain rate around $1/\tau$, a Maxwell fluid shows complex behavior [*Sumino et al.*, 2012]. We, thus, performed a series of experiments using a quasi-Maxwell fluid to understand the role of rheological transition on the disappearance of seismicity with depth.

2. Interpretation of the Rheology of Rocks Using τ

Figure 2 shows a schematic stress-strain history for loading and unloading on a Maxwell fluid. Under a slow deformation in which the strain rate is smaller than the inverse of relaxation time $\dot{\gamma} \ll 1/\tau$, a Maxwell fluid responds as a viscous fluid, and the strain remains after unloading, as shown by the circle and the blue arrow in Figure 2a. For a rapid deformation $\dot{\gamma} \gg 1/\tau$, the Maxwell fluid stores an elastic energy so that the strain rebounds, when unloading occurs (Figure 2c). This rebound can be a source of an earthquake. For an intermediate strain rate of $\dot{\gamma} \sim 1/\tau$, a certain fraction of the strain remains after unloading, as denoted in Figure 2b (red and blue arrows).

By comparing Figures 1 and 2, in which subduction velocity v_s does not depend on the depth, we infer that the relaxation time of the upper crust is sufficiently long so that the strain rate generated by the subducting slabs exceeds the inverse of the relaxation time $\dot{\gamma} \gg 1/\tau$, i.e., the upper crust is modeled as an elastic layer and earthquakes occur. In contrast, the relaxation time of most of the mantle is shorter than that of the upper crust so that $\dot{\gamma} \ll 1/\tau$, i.e., most of the mantle is modeled as an viscous layer, and earthquakes do not occur. Figure 2b suggests that earthquakes at the downdip limit of the seismogenic zone, which may be located within the lower crust or the shallow upper mantle, do not recover all of the strain accumulated in the interseismic duration.

3. Our Rock Analogue

For our rock analogue, we used a viscoelastic gel, known as a popular toy, slime. Our gel is a "quasi-Maxwell fluid" made by mixing polyvinyl alcohol and borax solutions. Stiffer gels are made by increasing the concentrations of both solutions. The density of the gel is 1.0×10^3 kg m^{-3}. Here we use the term quasi-Maxwell fluid for a material in which, under a rapid deformation, the strain is stored as an elastic energy; whereas for a slow deformation, the elastic energy dissipates viscously, as discussed in Figure 2.

Figure 3 shows the stress-strain histories for loading and unloading of our gel with $\tau = 12$ s and $G = 8.9$ kPa measured by a rheometer (Anton Paar MCR). Here τ and G are estimated by the dynamic viscoelasticity described below. A thin gel located between the two plates is sheared when monitoring the stress. We imposed four different and approximately constant shear strain rates on the same gel as denoted by numbers in the figure and then suddenly removed the imposed stress ($\sigma = 0$) at conditions denoted by

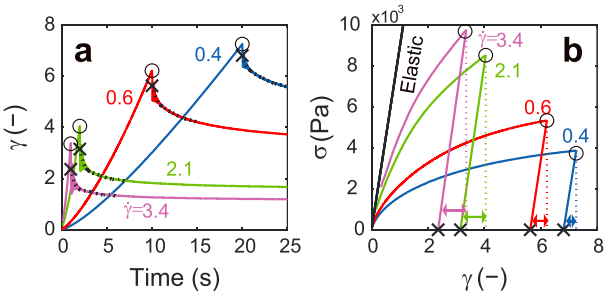

Figure 3. Rheological properties of our gel as a rock analogue, with $\tau = 12$ s and $G = 8.9$ kPa. (a) Time evolution of the strains of a gel under approximately constant shear strain rates and unloading. Black dotted curves are polynomial fits for the duration of the slow recovery. Crosses are intersections of black dotted curves and measured strains and are considered to be unrecoverable strains immediately after unloading. (b) Stress-strain curves of Figure 3a. The black line is an estimated elastic deformation using $G = 8.9$ kPa. Dotted lines indicate the stress drop assuming no recovery, and small arrows indicate the recovered strains. In Figures 3a and 3b, numbers denoted by the same color of curves indicate the shear strain rates. Circles indicate unloading.

the circles. Dotted lines in Figure 3b indicate stress drop without any recovery. First, the strain increases as time elapses. Following the removal of the imposed stress, some part of the strain recovers rapidly, and then recovery of the strain continues slowly (Figure 3a). Given that the measured strain oscillates during the rapid recovery, we determined the strain after rapid recovering using a polynomial fitting for the duration of the slow recovery, as denoted by black dotted curves (Figure 3a). The calculated strains are denoted in Figure 3 (black crosses).

Figure 3b shows that the measured lines for strain recovery after removing the stress are parallel to the black line estimated for elastic deformation by rigidity irrespective of imposed strain rates, suggesting that elastic rebound occurs. The elastically recovered strains are denoted by arrows in Figure 3b. Figure 3 also shows that the permanent strain remains even after the removal of the imposed stress. In Figure 3a, some part of the strain slowly recovers like an afterslip, but most of the strain remains. The permanent strain becomes larger for a slower deformation and for a long-time deformation. Such a permanent strain is a result of viscous deformation.

The stress-strain curves shown in Figures 2b and 3b are explained by a solution of the constitutive equation for a Maxwell fluid,

$$\dot{\gamma} = \frac{1}{G_a}\frac{d\sigma}{dt} + \frac{\sigma}{\eta_a} \tag{1}$$

where t is time. Assuming constant strain rate $\dot{\gamma} = \gamma/t$, where γ is a strain, which is applicable to both a subducting slab and our experiments, and integrating equation (1) with the initial condition of $\sigma = 0$ at $t = 0$, we obtain the strain-dependent stress

$$\sigma = \eta_a \dot{\gamma}(1 - e^{-\gamma/\dot{\gamma}\tau}). \tag{2}$$

Equation (2) indicates that the stress increases with strain and reaches an asymptotical value, $\lim_{\gamma\to\infty}\sigma = \eta\dot{\gamma}$. Figure 3b suggests that asymptotical values of stresses at the infinite strain increase with the strain rate $\dot{\gamma}$. In contrast, for a small strain, equation (2) indicates elastic deformation where $\lim_{\gamma\to 0}\sigma = G\gamma$.

Relaxation time and rigidity are measured by using the dynamic viscoelasticity [e.g., *Larson*, 1999], which is obtained by imposing a small-amplitude oscillatory shear on a sample,

$$\gamma(t) = \gamma_0 e^{i\omega t}, \tag{3}$$

where γ_0 is amplitude and ω is angular frequency.

The expected stress variation for a Maxwell body is obtained as a solution of equations (1) and (3),

$$\sigma(t) = (G' + iG'')\gamma_0 e^{i\omega t}, \tag{4}$$

where G' is in phase with the strain and represents the storage of elastic energy, while G'' is in phase with the strain rate and represents the viscous dissipation of energy; they are defined by

$$G'(\omega) = \frac{G\omega^2\tau^2}{1+\omega^2\tau^2},\ G''(\omega) = \frac{G\omega\tau}{1+\omega^2\tau^2}. \tag{5}$$

Figure 4a shows the dynamic viscoelasticity of a Maxwell fluid with the assumption that $G = 7 \times 10^{10}$ Pa and $\tau = \eta/G = 10^{10}$ s.

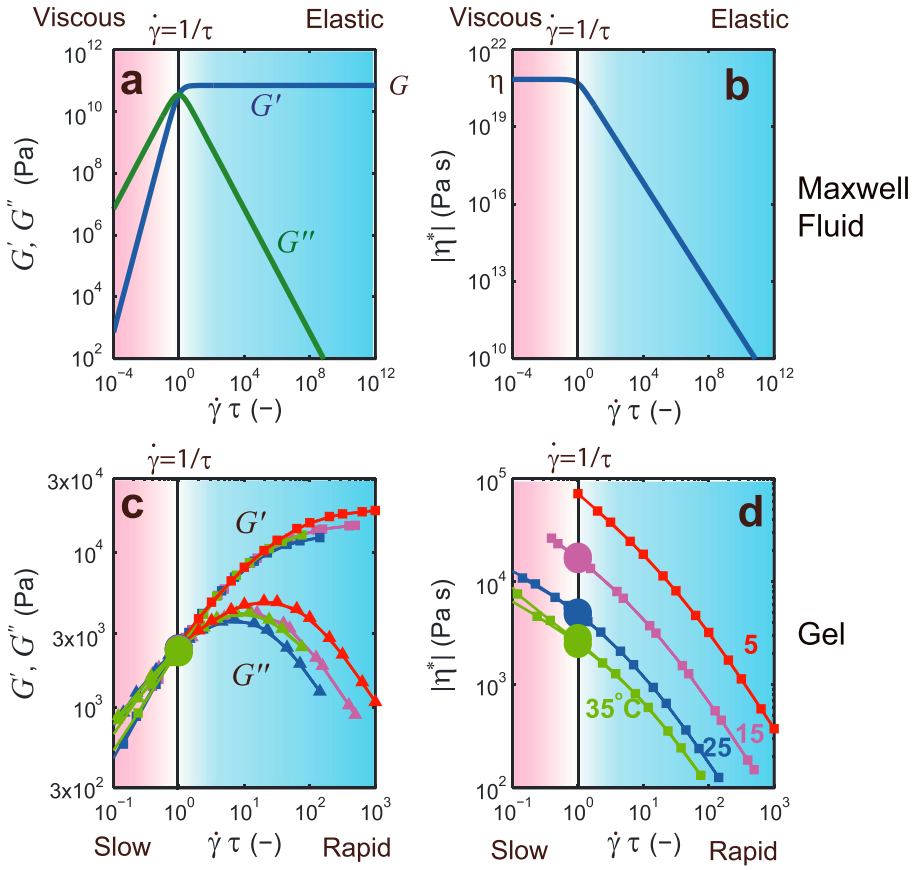

Figure 4. Comparison between the Maxwell fluid and our rock analogue. (a, b) Estimated storage G' and loss moduli G'' and the complex dynamic viscosity $|\eta^*|$ of the mantle, assuming a Maxwell fluid, calculated by equation (5). (c, d) Measured G' (squares) and G'' (triangles) and $|\eta^*|$ of the gel. Colors indicate the temperature difference as denoted by numbers with the same colors.

For a rapid deformation $\dot{\gamma} \gg 1/\tau$, $G' \gg G''$, the Maxwell fluid behaves like an elastic material with a rigidity G. Whereas for a slow deformation $\dot{\gamma} \ll 1/\tau$, $G' \ll G''$, the Maxwell fluid deforms viscously with a viscosity η. For $\dot{\gamma} \gg 1/\tau$, the magnitude of the complex viscosity, $|\eta^*| = \sqrt{G'^2 + G''^2}/\omega$, decreases (Figure 4b).

Figures 4c and 4d show the dynamic viscoelasticity of the gel used in our experiments, measured by a rheometer. The basic rheology of the gel is similar to that of a Maxwell fluid. We used the strain rate at which the storage and loss moduli become equal to calculate the relaxation time scale $\tau = 1/\dot{\gamma}|_{G'=G''}$, where $\dot{\gamma} = \omega/2\pi$. Given that the rheology of the gel is temperature dependent, we calculated the relaxation time at room temperature. We measured the relaxation time of the gel at 5, 15, 25, and 35°C and interpolated these values using the Arrhenius equation. We used two different gels with varying water concentrations. Both show similar profiles of G', G'', and $|\eta^*|$.

4. Experimental Method

Figure 3 shows that our gel simultaneously deforms viscously and elastically. However, it is not obvious whether the observed partial rebound in Figure 3 occurs during earthquakes observed on Earth. We next conducted shear deformation experiments with the apparatus shown in Figure 5 to simulate a situation in which a subducting plate deforms the viscoelastic crust/mantle (Figure 1). We simulated the difference in relaxation times by varying the shear rate. The acrylic tank has inner dimensions with a width of 0.3 m, height of 0.1 m, and a depth of 0.1 m, and is equipped with an acrylic slider with a length of 0.45 m. The slider is mounted to a stepping motor (Oriental Motor LAM4B40AW-6) and deforms the overlying gel at a constant velocity. The force required to move the slider is measured by a load cell (Kyowa LUX-B-1kN-ID) with a time resolution of 5×10^{-4} s and is recorded through an oscilloscope (Agilent 54624A) with a data length of 10^6 and sampling rate of 2–20 kHz, i.e., for a longer experiment, the sampling rate becomes low.

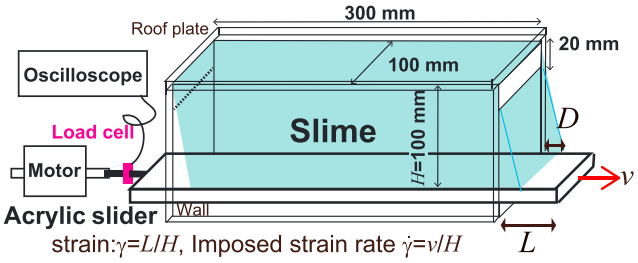

Figure 5. A schematic diagram of the experimental apparatus.

The measured force data are analyzed after reducing the time resolution to 2×10^{-3} and 4.2×10^{-3} s by averaging the data to compare the images from high-speed cameras taken at 500 and 240 frames per second (fps), respectively. The stress stored in the gel is obtained by dividing the force by the bottom area of the gel (0.1×0.3 m^2).

First, we filled the acrylic tank with a gel, then we put the roof plate on and waited at least 3 h so that any residual stress relaxed, which is observed by photoelasticity. We removed the walls at both sides of the tank so that the gel was surrounded by the front and back walls and the roof plate. We then started moving the slider as soon as possible after the removal of the sidewalls to prevent the gel from flowing. We moved the slider a total distance of $L = 0.12$ m to impose a total strain of $\gamma = 1.2$, with velocities in the range of $3 \times 10^{-4} < v < 3 \times 10^{-2}$ m s^{-1}. We here calculate the strain and strain rate by using the height of the gel H, $\gamma = L/H$ and $\dot{\gamma} = v/H$, respectively. We recorded the shear deformation of the gel with high-speed cameras. Ditect HAS-500 takes snapshots at 500 fps with a resolution of 1024×480 pixels and records for 4.2 s. Casio Exilim ZR-15 takes pictures at 240 fps with a resolution of 512×314 pixels and records the entire duration of each experiment. The images and force data are correlated by using a light-emitting diode connected to a function generator that regularly lights 2 s of every 4 s. The experimental tank is illuminated from behind. A seam of lights at the tank's middepth is evident as a thick dark line in Figures 6a, 7a, and 8a. To visualize the deformation, we suspended several particles in the gel. The particles have diameters of 6 mm and 2.5 mm. The density of the particle is similar to that of the gel, 1.0×10^3 kg m^{-3}, so that the relative motion between the particles and the surrounding gel is negligible. Recorded images were analyzed using MATLAB.

5. Experimental Results

5.1. Shear Deformations

We performed shear deformation experiments under various imposed strain rates, $\dot{\gamma}$. We found that deformation of the sheared gel depends on the imposed strain rate, $\dot{\gamma}$ (Figures 6–8 and Movies S1–S5).

Figure 6a and Movie S1 show the photograph of our gel before and after the deformation at a small imposed strain rate, $\dot{\gamma} = 3 \times 10^{-3}$ s^{-1}. The shape of entire gel changes, bubbles trapped in the gel are stretched as denoted by the pink circle, and the configuration of tracer particles embedded within the gel changes after

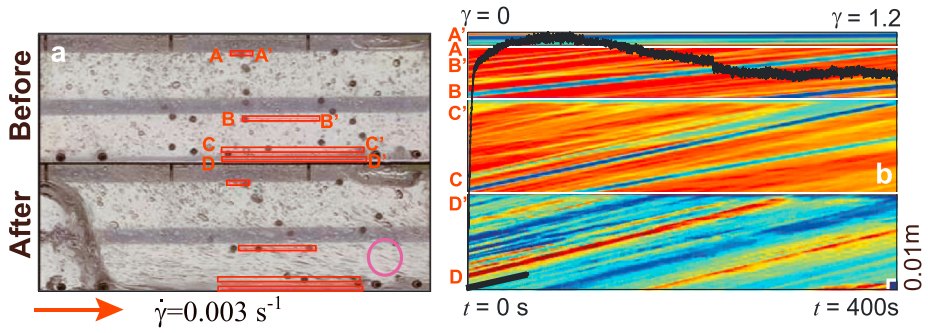

Figure 6. (a) Photographs of the gel at the start and end of the shear deformation experiment in the direction of the red arrow. The shear strain rate is 3×10^{-3} s^{-1}. Dark dots are particles, bubbles, and cracks. The pink circle shows a deformed bubble. A horizontal dark line at the middepth of the tank is the seam of lights. The curve at the left side in the bottom photograph is the edge of the gel. The vertical length scale of each photograph is 0.1 m. (b) Time evolution of the regions surrounded by red boxes in Figure 6a rotated by 90°. Corresponding regions are marked by letters of the alphabet, AA′–DD′. Time and strain increase to the right, $\gamma = \dot{\gamma}t$. The image is artificially colored to be recognizable. The bluish and reddish regions show darker and brighter regions in Figure 6a, respectively. Upward shifting trajectories indicate rightward migration in Figure 6a. The slope of the thick black line indicates the slider's velocity. The thin black curve shows the force required to move the slider. The blue marker at the bottom right corner is the length scale, 0.01 m.

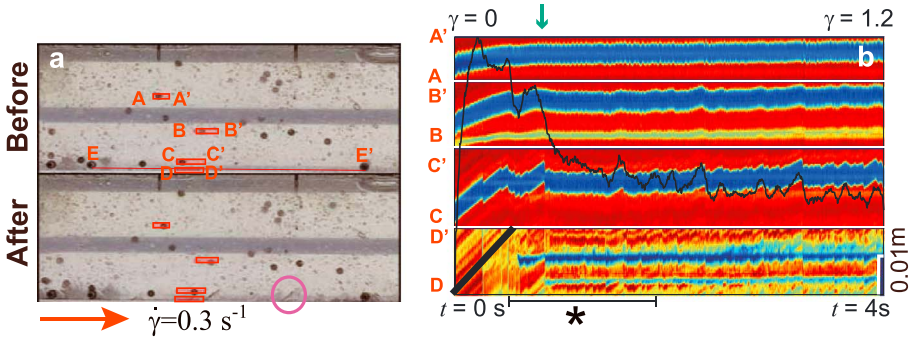

Figure 7. Same as for Figure 6 but with a rapid strain rate, $\dot{\gamma} = 0.3\ s^{-1}$. The pink circle shows a microcrack. The green arrow indicates a slip event. A close-up view of the range denoted by the asterisk is shown in Figure 9.

shear deformation. In contrast, when the imposed strain rate is high, $\dot{\gamma} = 0.3\ s^{-1}$, the gel does not deform, and the configuration of the bubbles and particles do not change significantly (Figure 7a and Movies S2 and S3). This is because the gel sometimes detaches from the underlying acrylic slider to release the accumulated strain, which may correspond to earthquakes in the natural system. We refer to these phenomena as slip events in the following. Some cracks appear with a different angle of stretched bubbles as denoted by the pink circle, suggesting the generation of microcracks associated with rupture propagation [e.g., *Vermilye and Scholz*, 1998; *Kim et al.*, 2004; *Andrews*, 2005].

The details of the deformation are visualized by the trajectory of tracer particles embedded within the gel. Figures 6b, 7b, and 8b show the time-dependent deformation of the gel in the red boxes denoted in Figures 6a, 7a, and 8a, respectively. Each red box was rotated 90° counterclockwise and was aligned in a rightward direction with time. Corresponding boxes are marked by letters of the alphabet, AA′–DD′. The image is artificially colored, and bluish regions show the dark regions in Figures 6a, 7a, and 8a, i.e., particles, bubbles, and cracks. In Figures 6b, 7b, and 8b, upward slopes indicate the rightward displacement of the gel visualized by particles embedded in the gel. The slope of the thick black line indicates the velocity of rightward displacement of the acrylic slider.

When the imposed strain rate is small, $\dot{\gamma} = 3 \times 10^{-3}\ s^{-1}$, Figure 6b (DD′, bottom) shows upward slopes of bluish and reddish regions with the same angle as the thick black line, indicating that the gel deforms with the slider at this depth, i.e., the bottom of the gel sticks to the slider and moves at the same velocity. The slope angles reduce for shallower panels, i.e., the top of the gel sticks to the roof of the tank and does not deform. The force required to move the slider shown by the thin black curve abruptly increases and then remains at approximately the same level. These characteristics and Movie S1 are interpreted as viscous deformation.

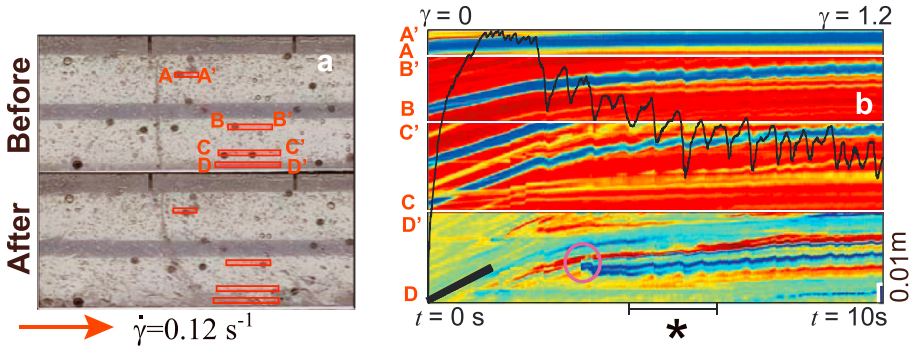

Figure 8. Same as for Figure 6 but with an intermediate strain rate, $\dot{\gamma} = 0.12\ s^{-1}$. The vertical gray curve in Figure 8a is a line of bubbles that shows the unrecoverable deformation. The pink circle shows a broadening microcrack. A close-up view of the range denoted by the asterisk is shown in Figure 10.

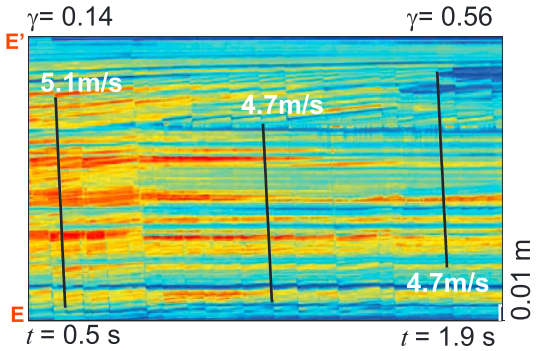

Figure 9. Same as Figure 7b (bottom) but showing a wider region of 0.2 m as denoted by E-E′ (Figure 7a) and a shorter time duration of 1.4 s as denoted by the asterisk in Figure 7. The black lines show traces of the rupture passages with calculated rupture velocities.

In contrast, when the imposed strain rate is high, $\dot{\gamma} = 0.3\ s^{-1}$ (Figure 7b), the slope of the bluish region is almost flat with some fluctuations, after the initial transient stage ($t > 0.5$ s). These fluctuations indicate slip events. During a slip event, a local detachment between the gel and the slider passes along the bottom plane of the gel in the reverse direction of the slider and releases the accumulated strain in the overlying gel (Movies S2 and S3). The detachment and release of the strain are recognized by the discontinuous drop of the bluish region, as denoted by the green arrow. This propagation of detachment is similar to a Schallamach wave [*Schallamach*, 1971; *Yamaguchi et al.*, 2011], a wrinkle-like slip pulse [*Andrews and Ben-Zion*, 1997], and is a kind of a failure process. In the panels of Figure 7b (AA′–CC′), amplitudes of fluctuations increase with depth, indicating that the coslip displacement decreases with the distance from the epicenter. In Figure 7b (DD′, bottom), some cracks newly appear, making the amplitude of fluctuation complicated. The fluctuation of the bluish region correlates with that of the thin black curve, showing that the accommodated stress in the gel is released by the slip events.

Propagation velocities of detachments, which correspond to the rupture velocity in seismology, are measured by visual observations. Figure 9 is the close-up view of Figure 7b in the time and strain range denoted by the asterisk at the EE′ plane in Figure 7a. Slopes of discontinuous displacements associated with slip events are consistent with the propagation velocity as traced in Figure 9 (black lines). The calculated velocity is approximately 5 m s^{-1}.

At the intermediate imposed strain rate of $\dot{\gamma} = 0.12\ s^{-1}$, slip events occur with increasing total deformation (Figure 8b). The loci of particles shown in the bluish regions continuously migrate up(right)ward, with intermittent down(left)ward movements. Some cracks appear and broaden around the bottom of the gel, identified by the appearance of a new bluish region as denoted by Figure 8b (pink circle). The force required to move the slider correlates with the fluctuation of the bluish region. The time and strain range denoted by the asterisk is enlarged in Figure 10. In Figures 10c and 10d, slip events occur repeatedly in a single stress drop event, as shown by the black arrows. However, the repeated slip events are observed as a single event by the displacement at shallow depth (Figure 10b). Displacements at the shallowest depth do not represent the slip events at the bottom of the gel (Figure 10a).

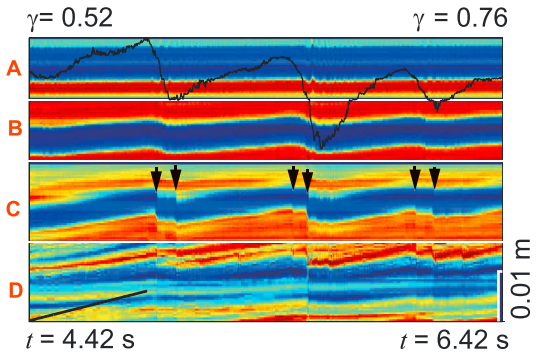

Figure 10. A close-up view of Figure 8b for a time window of 2 s, as denoted by the asterisk in Figure 8b. (a–d) Spatial enlargements within the red boxes shown in Figure 8a. Black arrows indicate the discontinuous deformation of gel showing the occurrence of slips.

5.2. Time Variation of the Stress in the Gel

Figure 11 compares histories of stress in the gel, a ratio of the measured force required to move the slider to the bottom area of the gel. Colors indicate the differences in imposed strain rates, $\dot{\gamma}$ (Table 1). When the imposed strain rate $\dot{\gamma}$ is sufficiently high, first, the stress increases with the strain, reaching a maximum, and then it fluctuates in association with the slip events. Concurrently, there is a secular stress decrease, indicating that the stress does not increase despite the increase in total strain. In contrast, when the imposed strain rate $\dot{\gamma}$ is sufficiently small, the amplitude of the stress fluctuations is also small. The observed maximum stresses for experiments with slip events are larger than those for experiments without slip events.

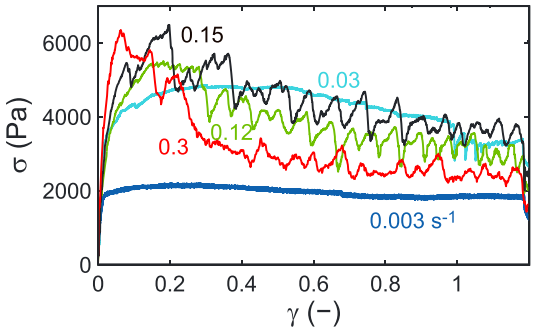

Figure 11. The stress variation required to move the slider as a function of strain. Colors indicate the different strain rates and correspond to those listed in Table 1.

The apparently thick width of the curve for $\dot{\gamma} = 3 \times 10^{-3}$ s^{-1} is originated from the low resolution of the data to acquire long time.

These characteristics become obvious in Figure 12, which summarizes the stress variation as a function of the normalized strain rate, $\dot{\gamma}\tau$. Different colors and symbols indicate the imposed strain rates and gels, respectively (Table 1). For $\dot{\gamma}\tau < 1$, the observed stress increases with $\dot{\gamma}\tau$ and with small variations, suggesting a viscous deformation in which stress is proportional to the strain rate. For $\dot{\gamma}\tau > 1$, in contrast, the maximum stress is an approximately constant $\sigma \sim 6$ kPa, while the minimum and average stress decreased with $\dot{\gamma}\tau$. These results suggest that the adhesive stress which sticks the gel to the slider is approximately $\sigma_a \sim 6$ kPa and decreases with repeated slip events.

6. Discussion

6.1. Unrecoverable Displacements After Slip Events

From the above experimental results, we consider that the threshold of a slip event is when the stress within the gel exceeds the adhesive stress that sticks the gel to the slider, i.e., $\sigma = \sigma_a$. The stress in a deforming gel at strain rate $\dot{\gamma}$ at elapsed time t is $\sigma = G(\dot{\gamma})\dot{\gamma}t$. Here the elapsed time should be shorter than the relaxation time scale $t < \tau$. Thus, the condition for slip events can be rewritten as follows:

$$\dot{\gamma}\tau \cdot G(\dot{\gamma}) > \sigma_a. \tag{6}$$

Figure 13a compares $\dot{\gamma}\tau \cdot G(\dot{\gamma})/\sigma_a$ with D/L, where D/L is the ratio of total displacement of the particles closest to the slider D to the total displacement of the slider $L = 0.12$ m (Figure 5). We calculated the rigidity by $G(\dot{\gamma}) = \sqrt{G'^2 + G''^2}$ and assumed $\sigma_a = 6 \times 10^3$ Pa, which is approximately the maximum measured stress shown in Figure 12. Symbols and colors show the different gels and imposed strain rates (Table 1).

Table 1. Experimental Conditions[a]

Velocity (mm s^{-1})	τ (s)	G (×10^4 Pa)	D (mm)	Height (mm)	D/L (-)	Color		
3.0	26	3.9	132	6	1.11	light blue	*	
7.4	18	1.5	54	6	0.46	pink	*	
0.3	25	–	96	7	0.81	blue	*	Figure 6
11.9	19	2.8	45	3	0.38	green	*	Figure 8
29.7	20	1.5	12	5	0.10	red	*	
14.8	36	2.4	24	4	0.20	black	*	
29.7	41	2.8	11	7	0.10	red	*	Figure 7
7.4	11	–	130	7	1.10	pink	◇	
14.8	18	2.5	71	12	0.60	black	◇	
29.7	13	2.8	43	5	0.36	red	◇	
11.9	21	–	96	4	0.81	green	◇	
8.9	13	1.8	100	5	0.84	yellow	◇	
3.0	11	–	100	9	0.85	light blue	◇	
1.5	15	–	102	6	0.86	blue	◇	

[a]Velocity: Slider velocity. τ: Relaxation time of the gel at room temperature. G: Rigidity calculated from the rupture velocities (Figure 9). D: Total travel distance of the particle nearest the bottom. Height: Height of the particle from the bottom used to measure D. D/L: Normalized D by the total displacement of the slider $L = 0.12$. Colors and symbols correspond to Figures 11–13. Experiments were conducted in the order listed in this table. Rheological properties of the gel denoted by asterisk are shown in Figures 4c and 4d.

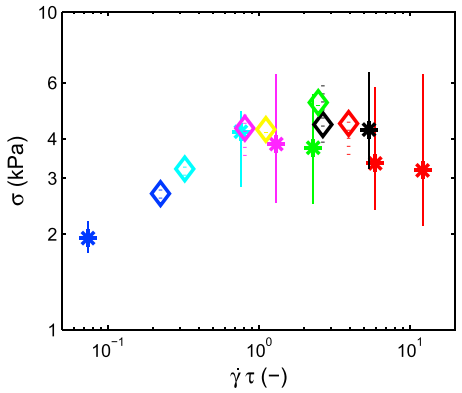

Figure 12. Summary of the stress variation shown in Figure 11 as a function of the normalized strain rate. Error bars indicate the measured stress ranges after the stress becomes maximum. Symbols indicate the average stress after the stress becomes maximum. Colors and symbols indicate different strain rates and gels, respectively, and correspond to those listed in Table 1.

If the imposed strain rate is small, $\dot{\gamma}\tau \cdot G(\dot{\gamma})/\sigma_a < 1$, D/L is around unity, indicating that the bottom of the gel continuously adheres to the slider such that viscous deformation takes place. Conversely, when the imposed strain rate is high, $\dot{\gamma}\tau \cdot G(\dot{\gamma})/\sigma_a > 1$, D/L gradually decreases. This fact represents the increase in the total elastic rebound caused by slip events. Thus, we conclude that $\dot{\gamma}\tau \cdot G(\dot{\gamma})/\sigma_a$ is a measure of the occurrence of slip events.

Next, we explain the trend of decreasing D/L at the regime $\dot{\gamma}\tau \cdot G(\dot{\gamma})/\sigma_a > 1$, assuming a Maxwell fluid. Here L is the summation of interslip displacements, $L = nL_s$, where L_s is an inter-slip displacement before a slip event, and n is the number of slip events that occurred during each experiment. A critical interslip strain for causing a slip event $L_s/H = \gamma_{cs}$ is estimated from equation (2) with the relation of $\eta_a = \tau G_a$

$$\gamma_{cs} = -\dot{\gamma}\tau \log\left(1 - \frac{1}{\dot{\gamma}\tau}\frac{\sigma_a}{G_a}\right). \tag{7}$$

On the other hand, D is the summation of unrecoverable displacements after slip events, $D = nD_s$. Using the interslip critical strain, an unrecoverable displacement is written as $D_s/H = \gamma_{cs} - \sigma_a/G_a$, where σ_a/G_a is a strain recoverable by an elastic rebound as associated with a slip event. Thus, we obtain

$$\frac{D}{L} = \frac{nD_s/H}{nL_s/H} = 1 + \frac{\sigma_a}{\dot{\gamma}\tau G_a \log\left(1 - \frac{1}{\dot{\gamma}\tau}\frac{\sigma_a}{G_a}\right)}. \tag{8}$$

Figure 13a (black curve) shows that D/L as a function of $\dot{\gamma}\tau \cdot G_a/\sigma_a$ as calculated by equation (8) explains the trend of experiments well. We thus conclude that there is a regime in which slip events occur, but some part of the strain remains after slip events, and the regime appears around $\dot{\gamma}\tau \cdot G(\dot{\gamma})/\sigma_a \sim 1$.

6.2. Rupture Velocities

Next, we consider the rupture velocity around $\dot{\gamma}\tau \cdot G(\dot{\gamma})/\sigma_a \sim 1$. Figure 13b summarizes the rupture velocities of slip events as measured by a method similar to that used for Figure 9. We used images of the bottom of

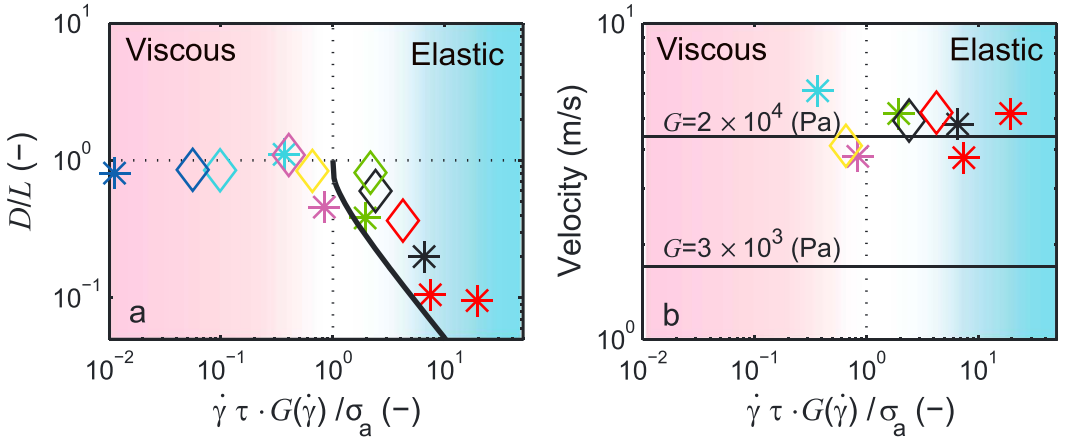

Figure 13. Transition from the viscous to the elastic regime as the imposed strain rate increases. (a) Total displacement of the particles closest to the slider, D, normalized by the total displacement L = 0.12 m (Figure 5), as a function of the normalized strain rate from equation (6). The black curve is calculated by equation (8). (b) The measured rupture velocity at the bottom of the gel, which is calculated from similar slopes of the black lines shown in Figure 9. Horizontal black lines indicate the shear wave velocity for rigidities of 3×10^3 and 2×10^4. In Figures 13a and 13b, we assume $\sigma_a = 6 \times 10^3$ Pa. Symbols and colors correspond to those listed in Table 1.

the gels taken every 2 ms. We traced the rupture propagation automatically and removed any improper traces manually. Note that not all ruptures can be traced. Ruptures that are difficult to trace but that can be tracked visually also show similar velocities (Figure 9). We plotted the average rupture velocity in Figure 13b.

The two black lines in Figure 13b indicate the shear wave velocities for the maximum rigidity of $G(\dot{\gamma}) \sim 2 \times 10^4$ Pa and for a rigidity of $G(\dot{\gamma}) \sim 3 \times 10^3$ Pa when the strain rate corresponds to the inverse of the relaxation time scale (Figure 4c). The colors and symbols correspond to those in Figure 13a. Figure 13b indicates that the measured rupture velocities are independent of $\dot{\gamma}\tau \cdot G(\dot{\gamma})/\sigma_a$ and similar to the shear wave velocity estimated from the maximum rigidity, $G(\dot{\gamma}) = 2 \times 10^4$ Pa (Figure 4c). This is because the stress changes caused by ruptures occur instantaneously. Rapid stress change propagates at a shear wave velocity. Since ruptures always propagate at a shear wave velocity, irrespective of the amount of viscous relaxation, we regard the slip events observed in our experiments corresponds to earthquakes in the natural system.

6.3. Implication for the Real Faulting System
6.4. Small Magnitudes at a Depth

Our experiments reveal the threshold for occurrences of slip events on a Maxwell fluid: $\dot{\gamma}\tau \cdot G(\dot{\gamma})/\sigma_a > 1$. Above this threshold, slip events occur; beneath this threshold, a Maxwell fluid deforms viscously, and slip events do not occur. Around the threshold, only a certain fraction of the displacement that accumulates in the interseismic duration is recovered by elastic rebound; the other part remains as unrecoverable displacements. Even in this regime, the propagation velocity of the rupture is consistent with the shear wave velocity. From these results, we infer that some earthquakes could rebound only some part of interseismic displacement. In this section, we apply these experimental results to a subduction zone.

In our experiments, we calculated the interseismic shear rate using the height of the gel, v/H, in which the shear rate varies with the slider velocity. In a real faulting system in a subduction zone, however, subduction velocity, v_s, is constant; whereas the relaxation time, $\tau \sim \eta_a/G_a$, can vary, as we discussed using Figure 1. Length scales to calculate the shear rate also vary. The subducting plate sticks to the hanging wall through localized asperities determining the fault length scale W, which are surrounded by an aseismically creeping area [e.g., *Lay et al.*, 1982].

The fault length is related to the seismic moment $M \sim GD_sW^2$, where D_s is a coseismic displacement (an elastic rebound). It is known that the seismic moment is proportional to the 3/2 power of the rupture area, indicating $M \sim \Delta\sigma W^3$, with a constant stress drop $\Delta\sigma$ [*Aki*, 1972; *Kanamori and Anderson*, 1975]. Using $GD_sW^2 \sim \Delta\sigma W^3$, we obtain $\Delta\sigma \sim GD_s/W$, i.e., $\gamma \sim D_s/W$. From this scaling, we expect that the extent of stress accumulation surrounding a fault is scaled with the fault size W, and we obtain $\dot{\gamma} = v_s/W \propto M^{-1/3}$. Thus, the imposed strain rates for larger faults become smaller than those for smaller ones, even for the same subduction velocity.

Substituting $\dot{\gamma} = v_s/W$ into equation (6), the condition for earthquakes is rewritten as

$$\frac{v_s\eta}{\sigma_a} > W \propto M^{1/3}. \tag{9}$$

In equation (9), we used η instead of τG_a. This is because we do not know τ. We assume $\eta_a \sim \eta$, where η is the observed viscosity. Here the subduction velocity, v_s, does not vary significantly. Thus, equation (9) shows that the combination of viscosity η and adhesive stress σ_a regulates the maximum size of earthquakes. In a deeper part, where the viscosity may be lower than in a shallower part, a fault with a small length and low adhesive stress can cause earthquakes.

Equation (9) qualitatively explains the characteristics of slow earthquakes. Slow earthquakes are observed beneath the seismogenic zone [e.g., *Lay et al.*, 2012], where the viscosity of surrounding rocks may be lower because of the high temperature. Observed magnitudes of individual slow earthquakes are much smaller than those of ordinary earthquakes [*Beroza and Ide*, 2011]. Estimated stress drops for slow earthquakes are smaller than those for ordinary earthquakes [*Brodsky and Mori*, 2007].

If slow earthquakes occur around the threshold, some part of the interseismic displacements remains after slip events. It is known that there are two peak depths for tremors, and up-dip peaks correlate with geodetically observed slow slips, but downdip peaks do not [*Wech et al.*, 2009]. One possible explanation is the limit of GPS detection levels. An alternative interpretation is that the recoverable displacements become smaller with increasing depth.

6.5. The Low Frequency of Slow Earthquakes

The other characteristic of slow earthquakes is their low frequency [e.g., *Beroza and Ide*, 2011; *Obara*, 2011]. Complex frictional law can explain a slow rupture velocity which may be observed at low frequency [e.g., *Perfettini and Ampuero*, 2008; *Suzuki and Yamashita*, 2009; *Shibazaki et al.*, 2012; *Colella et al.*, 2013; *Matsuzawa et al.*, 2013]. Our experiments suggest an alternative interpretation. In Figure 10 and Movies S4 and S5, some slip events (black arrows) occur successively and are observed as a single slip event with a slow rupture velocity at shallow depth. This result brings to mind the observation that slow slips are associated with tremors, and the total slip is explained by the summation of the tremors [*Rogers and Dragert*, 2003; *Hiramatsu et al.*, 2008].

7. Concluding Remarks

We performed a series of shear deformation experiments using a quasi-Maxwell fluid above a sliding plate with various shear rates. Under a rapid deformation, the quasi-Maxwell fluid occasionally detaches from the underlying sliding plate and releases the accumulated strain. The local detachment propagates at a shear wave velocity similar to real earthquakes. In contrast, under a slow deformation, the quasi-Maxwell fluid sticks to the sliding plate and deforms viscously. Around the threshold, the detachment propagates at a shear wave velocity, but only some part of the accumulated strain recovers. Another part remains as an unrecoverable strain. The threshold is described by the combination of the shear rate, $\dot{\gamma}$, the relaxation time, τ, the rigidity, G, and the adhesive stress, σ_a, as shown in equation (6).

We applied these experimental results to a hanging wall deformed by a subducting slab. In the shallower region, the hanging wall behaves as an elastic layer, so that the interseismic displacement is intermittently recovered by earthquakes. In the deeper part, the hanging wall behaves as a viscous layer and descends with the subducting slab. At an intermediate depth, some part of the inter-seismic displacement is recovered by the elastic rebound generating seismicity, but another part remains and subducts together with the slab. The threshold is described by a combination of the subduction velocity, v_s, the viscosity of the hanging wall, η, the fault length, W, and the adhesive stress σ_a, as shown in equation (9).

This threshold indicates that if the viscosity of the hanging wall becomes smaller with depth by higher temperature, the maximum size of earthquakes also becomes smaller with depth. This hypothesis is consistent with observations in which slow earthquakes characterized by small magnitudes occur at the downdip limit of the seismogenic zone. Our experimental results provide a possible visual image of slow earthquakes.

Acknowledgments

We thank Hiroyuki Noda for his review and Osamu Kuwano for his helpful advice on technical issues. Movies supporting Figures 6–10 are available as supporting information. The original data for Figure 13 are listed in Table 1. This work was supported by KAKENHI 23654155.

References

Aki, K. (1972), Earthquake mechanism, *Tectonophysics*, *13*, 423–446.

Ando, R., N. Takeda, and T. Yamashita (2012), Propagation dynamics of seismic and aseismic slip governed by fault heterogeneity and Newtonian rheology, *J. Geophys. Res.*, *117*, B11308, doi:10.1029/2012JB009532.

Andrews, D. J. (2005), Rupture dynamics with energy loss outside the slip zone, *J. Geophys. Res.*, *110*, B01307, doi:10.1029/2004JB003191.

Andrews, D. J., and Y. Ben-Zion (1997), Wrinkle-like slip pulse on a fault between different materials, *J. Geophys. Res.*, *102*, 553–571.

Baumberger, T., C. Caroli, and O. Ronsin (2002), Self-healing slip pulses along a gel/glass interface, *Phys. Rev. Lett.*, *88*, 075,509.

Beroza, G. C., and S. Ide (2011), Slow earthquakes and nonvolcanic tremor, *Annu. Rev. Earth Planet. Sci.*, *39*, 271–296.

Bilek, S. L., and T. Lay (1999), Rigidity variations with depth along interplate megathrust faults in subduction zones, *Nature*, *400*, 443–446.

Brodsky, E. E., and J. Mori (2007), Creep events slip less than ordinary earthquakes, *Geophys. Res. Lett.*, *34*, L16309, doi:10.1029/2007GL030917.

Brune, J. N., S. Brown, and P. A. Johnson (1993), Rupture mechanism and interface separation in foam rubber models of earthquakes: A possible solution to the heat flow paradox and the paradox of large overthrusts, *Tectonophysics*, *218*, 59–67.

Burgmann, R., and G. Dresen (2008), Rheology of the lower crust and upper mantle: Evidence from rock mechanics, geodesy, and field observations, *Annu. Rev. Earth Planet. Sci.*, *36*, 531–567.

Colella, H. V., J. H. Dieterich, and K. Richards-Dinger (2013), Spatial and temporal patterns of simulated slow slip events on the Cascadia megathrust, *Geophys. Res. Lett.*, *40*, 5101–5107, doi:10.1002/grl.50984.

Corbi, F., F. Funiciello, C. Faccenna, G. Ranalli, and A. Heuret (2011), Seismic variability of subduction thrust faults: Insights from laboratory models, *J. Geophys. Res.*, *116*, B06304, doi:10.1029/2010JB007993.

Corbi, F., F. Funiciello, M. Moroni, Y. van Dinther, P. M. Mai, L. A. Dalguer, and C. Faccenna (2013), The seismic cycle at subduction thrusts: 1. Insights from laboratory models, *J. Geophys. Res. Solid Earth*, *118*, 1483–1501, doi:10.1029/2012JB009481.

Dziewonski, A. M., and D. L. Anderson (1981), Preliminary reference Earth model, *Phys. Earth Planet. Inter.*, *25*, 297–356.

Freed, A. M., R. Burgmann, E. Calais, and J. Freymueller (2006), Stress-dependent power-law flow in the upper mantle following the 2002 Denali, Alaska, earthquake, *Earth Planet. Sci. Lett.*, *252*, 481–489.

Hilairet, N., B. Reynard, Y. Wang, I. Daniel, S. Merkel, N. Nishiyama, and S. Petitgirard (2007), High-pressure creep of serpentine, interseismic deformation, and initiation of subduction, *Science*, *318*, 1910–1912.

Hilley, G. E., K. M. Johnson, M. Wang, Z. Shen, and R. Burgmann (2009), Earthquake-cycle deformation and fault slip rates in northern Tibet, *Geology*, *37*, 31–34.

Hiramatsu, Y., T. Watanabe, and K. Obara (2008), Deep low-frequency tremors as a proxy for slip monitoring at plate interface, *Geophys. Res. Lett.*, *35*, L13304, doi:10.1029/2008GL034342.

Hirauchi, K., I. Katayama, S. Uehara, M. Miyahara, and Y. Takai (2010), Inhibition of subduction thrust earthquakes by low-temperature plastic flow in serpentine, *Earth Planet. Sci. Lett.*, *295*, 349–357.
Hirschmann, M., and D. Kohlstedt (2012), Water in Earth's mantle, *Phys. Today*, *65*, 40–45.
Hyndman, R. D. (2013), Downdip landward limit of Cascadia great earthquake rupture, *J. Geophys. Res. Solid Earth*, *118*, 5530–5549, doi:10.1002/jgrb.50390.
Ito, Y., K. Obara, T. Matsuzawa, and T. Maeda (2009), Very low frequency earthquakes related to small asperities on the plate boundary interface at the locked to aseismic transition, *J. Geophys. Res.*, *114*, B00A13, doi:10.1029/2008JB006036.
Kanamori, H., and D. L. Anderson (1975), Theoretical basis of some empirical relations in seismology, *Bull. Seismol. Soc. Am.*, *65*, 1073–1095.
Kim, Y., D. C. P. Peacock, and D. J. Sanderson (2004), Fault damage zones, *J. Struct. Geol.*, *26*, 503–517.
Kohlstedt, D. L., B. Evans, and S. J. Mackwell (1995), Strength of the lithosphere: Constraints imposed by laboratory experiments, *J. Geophys. Res.*, *100*, 17,587–17,602.
Kuwano, O., and T. Hatano (2011), Flash weakening is limited by granular dynamics, *Geophys. Res. Lett.*, *38*, L17305, doi:10.1029/2011GL048530.
Larson, R. (1999), *The Structure and Rheology of Complex Fluids*, 663 pp., Oxford Univ. Press, Oxford.
Latour, S., A. Schubnel, S. Nielsen, R. Madariaga, and S. Vinciguerra (2013a), Characterization of nucleation during laboratory earthquakes, *Geophys. Res. Lett.*, *40*, 5064–5069, doi:10.1002/grl.50974.
Latour, S., C. Voisin, F. Renard, E. Larose, S. Catheline, and M. Campillo (2013b), Effect of fault heterogeneity on rupture dynamics: An experimental approach using ultrafast ultrasonic imaging, *J. Geophys. Res. Solid Earth*, *118*, 5888–5902, doi:10.1002/2013JB010231.
Lay, T., H. Kanamori, and L. Ruff (1982), The asperity model and nature of large subduction zone earthquakes, *Earthquake Pred. Res.*, *1*, 3–71.
Lay, T., H. Kanamori, C. J. Ammon, K. D. Koper, A. R. Hutko, L. Ye, H. Yue, and T. M. Rushing (2012), Depth-varying rupture properties of subduction zone megathrust faults, *J. Geophys. Res.*, *117*, B04311, doi:10.1029/2011JB009133.
Matsuzawa, T., B. Shibazaki, K. Obara, and H. Hirose (2013), Comprehensive model of short- and long-term slow slip events in the Shikoku region of Japan, incorporating a realistic plate configuration, *Geophys. Res. Lett.*, *40*, 5125–5130, doi:10.1002/grl.51006.
Mitrovica, J. X., and A. M. Forte (2004), A new inference of mantle viscosity based upon joint inversion of convection and glacial isostatic adjustment data, *Earth Planet. Sci. Lett.*, *255*, 177–189.
Muto, J., B. Shibazaki, Y. Ito, T. Iinuma, M. Ohzono, T. Matsumoto, and T. Okada (2013), Two-dimensional viscosity structure of the northeastern Japan islands arc-trench system, *Geophys. Res. Lett.*, *40*, 4604–4608, doi:10.1002/grl.50906.
Nakata, R., R. Ando, T. Hori, and S. Ide (2011), Generation mechanism of slow earthquakes: Numerical analysis based on a dynamic model with brittle-ductile mixed fault heterogeneity, *J. Geophys. Res.*, *116*, B08308, doi:10.1029/2010JB008188.
Nishimura, T., and W. Thatcher (2003), Rheology of the lithosphere inferred from postseismic uplift following the 1959 Hebgen Lake earthquake, *J. Geophys. Res.*, *108*(B8), 2389, doi:10.1029/2002JB002191.
Noda, H., and N. Lapusta (2013), Stable creeping fault segments can become destructive as a result of dynamic weakening, *Nature*, *493*, 548–521.
Nur, A., and G. Mavko (1974), Postseismic viscoelastic rebound, *Science*, *183*, 204–206.
Obara, K. (2011), Characteristics and interactions between non-volcanic tremor and related slow earthquakes in the Nankai subduction zone, southwest Japan, *J. Geodyn.*, *52*, 229–248.
Obara, K., S. Tanaka, T. Maeda, and T. Matsuzawa (2010), Depth-dependent activity of non-volcanic tremor in southwest Japan, *Geophys. Res. Lett.*, *37*, L13306, doi:10.1029/2010GL043679.
Oleskevich, D. A., R. D. Hyndman, and K. Wang (1999), The updip and downdip limits to great subduction earthquakes: Thermal and structural models of Cascadia, south Alaska, SW Japan, and Chile, *J. Geophys. Res.*, *104*, 14,965–14,991.
Perfettini, H., and J. Ampuero (2008), Dynamics of a velocity strengthening fault region: Implications for slow earthquakes and postseismic slip, *J. Geophys. Res.*, *113*, B09411, doi:10.1029/2007JB005398.
Pollitz, F. F. (2003), Transient rheology of the uppermost mantle beneath the Mojave Desert, California, *Earth Planet. Sci. Lett.*, *215*, 89–104.
Rogers, G., and H. Dragert (2003), Episodic tremor and slip on the cascadia subduction zone: The chatter of silent slip, *Science*, *300*, 1942–1943.
Rousset, B., S. Barbot, J. Avouac, and Y.-J. Hsu (2012), Postseismic deformation following the 1999 Chi-Chi earthquake, Taiwan: Implication for lower-crust rheology, *J. Geohpys. Res.*, *117*, B12405, doi:10.1029/2012JB009571.
Savage, J. C. (1983), A dislocation model of strain accumulation and release at a subduction zone, *J. Geophys. Res.*, *88*, 4984–4996.
Schallamach, A. (1971), How does rubber slide?, *Wear*, *17*, 301–312.
Shibazaki, B., K. Obara, T. Matsuzawa, and H. Hirose (2012), Modeling of slow slip events along the deep subduction zone in the Kii Peninsula and Tokai regions, southwest Japan, *J. Geophys. Res.*, *117*, B06311, doi:10.1029/2011JB009083.
Sumino, Y., H. Shibayama, T. Yamaguchi, T. Kajiya, and M. Doi (2012), Failure of film formation of viscoelastic fluid: Dynamics of viscoelastic fluid in a partially filled horizontally rotating cylinder, *Phys. Rev. E*, *85*, 046,307.
Suzuki, T., and T. Yamashita (2009), Dynamic modeling of slow earthquakes based on thermoporoelastic effects and inelastic generation of pores, *J. Geophys. Res.*, *114*, B00A04, doi:10.1029/2008JB006042.
Thatcher, W., T. Matsuda, T. Kato, and J. B. Rundle (1980), Lithospheric loading by the 1896 Riku-u Earthquake, northern Japan: Implications for plate flexure and asthenospheric rheology, *J. Geophys. Res.*, *85*, 6429–6435.
Tichelaar, B. W., and L. J. Ruff (1983), Depth of seismic coupling along subduction zones, *J. Geophys. Res.*, *98*, 2017–2037.
Ujiie, K., H. Tanaka, T. Saito, A. Tsutsumi, J. J. Mori, J. Kameda, E. E. Brodsky, F. M. Chester, N. Eguchi, and S. Toczko (2013), Low coseismic shear stress on the Tohoku-Oki megathrust determined from laboratory experiments, *Science*, *342*, 1211–1214.
Vermilye, J. M., and C. H. Scholz (1998), The process zone: A microstructural view of fault growth, *J. Geophys. Res.*, *103*, 12,223–12,237.
Wang, K., Y. Hu, and J. He (2012), Deformation cycles of subduction earthquakes in a viscoelastic Earth, *Nature*, *484*, 327–332.
Wech, A. G., K. C. Creager, and T. I. Melbourne (2009), Seismic and geodetic constraints on Cascadia slow slip, *J. Geophys. Res.*, *114*, B10316, doi:10.1029/2008JB006090.
Yamaguchi, T., M. Morishita, M. Doi, T. Hori, H. Sakaguchi, and J. Ampuero (2011), Gutenberg-richter's law in sliding friction of gels, *J. Geophys. Res.*, *116*, B12306, doi:10.1029/2011JB008415.
Yamasaki, T., and T. Seno (2005), High strain rate zone in central Honshu resulting from the viscosity heterogeneities in the crust and mantle, *Earth Planet. Sci. Lett.*, *232*, 13–27.